ACS NANO

www.acsnano.org

Subsurface Vacancy Engineering Enables Atomically Clean and Oxidation-Resistant Copper Interfaces for Anode-Free Lithium Metal Batteries

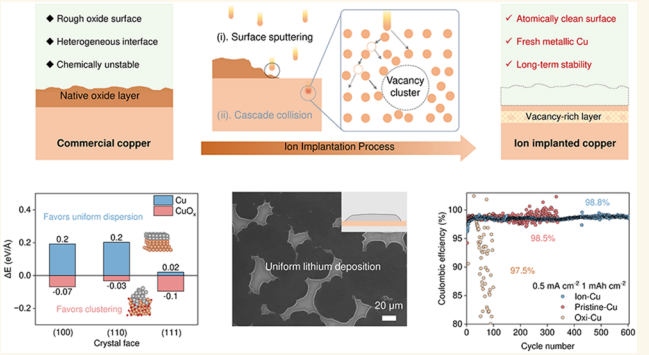
Yue Li,[⊥] Xuanguang Ren,[⊥] Xueting Feng,[⊥] Lingcheng Kong,[⊥] Fengping Luo, Yang Xu, Liu Qian, Yusheng Ye,* Ziqiang Zhao,* Xin Gao,* and Jin Zhang*

Cite This: *ACS Nano* 2026, 20, 18688−18699

Read Online

ACCESS | Metrics & More | Article Recommendations | Supporting Information

ABSTRACT: **Interfaces govern reaction pathways and stability in electrochemical systems, yet creating clean, well-defined metal interfaces at scale remains challenging. In anode-free lithium metal batteries (AFLMBs), the current-collector interface is decisive for lithium nucleation and solid electrolyte interphase (SEI) formation, and ideally should support efficient charge transport, uniform reaction distribution, and long-term chemical and structural stability. Here we report an ion-implantation strategy that produces an atomically clean and oxidation-resistant copper interface. Implanting copper ions into commercial foils removes the native oxide while generating subsurface vacancy clusters directly beneath the surface—an atomic-scale modification that does not increase the collector thickness but fundamentally alters interfacial chemistry. Experiments and multiscale simulations reveal that these vacancies act as strong oxygen traps, preventing reoxidation, enhancing interfacial conductivity, and guiding the formation of an ultrathin, Li_2O-enriched SEI that promotes uniform lithium deposition and suppresses parasitic reactions. Applied in AFLMBs, the engineered current collectors deliver long-term stability with a Coulombic efficiency of 98.8% over 600 cycles under lean-electrolyte conditions. These findings demonstrate atomic-scale interface control of copper current collectors as a route toward stable and practical lithium metal batteries.**



KEYWORDS: *anode-free lithium metal batteries, copper current collector, ion implantation, subsurface vacancies, oxidation resistance, solid electrolyte interphase, interface engineering*

Interfaces play a critical role in determining the performance and longevity of electrochemical systems from catalysis to energy storage. At these boundaries, charge transfer occurs, reaction selectivity is defined, and the degradation process initiates.[1] Achieving an ideal interface, characterized by efficient charge transport, uniform reaction distribution, and long-term chemical and structural stability, is essential for advancing next-generation electrochemical technologies. To this end, interface engineering strategies that modulate the surface wettability, nucleation dynamics, and interfacial kinetics have been widely explored.[2,3]

Anode-free lithium metal batteries (AFLMBs) have recently emerged as a compelling architecture for high-energy-density storage. By dispensing with a conventional anode and plating lithium directly onto a bare copper current collector (CuCC) during initial charging, AFLMBs offer simplified construction, reduced cost, and high gravimetric energy densities.[4−6] However, the absence of a host anode renders lithium plating highly sensitive to interfacial conditions at the CuCC, where dendritic growth, unstable solid electrolyte interphase (SEI) formation, and irreversible lithium loss often lead to rapid performance degradation and poor cycle life.[7−11]

Received: February 13, 2026
Revised: June 8, 2026
Accepted: June 9, 2026
Published: June 22, 2026



ACS Publications

© 2026 American Chemical Society

Downloaded from pubs.acs.org/ancac3/article-pdf/20/26/18688/6518791/1/acsnano.6c02968.pdf by PEKING UNIV user on 06 November 2026

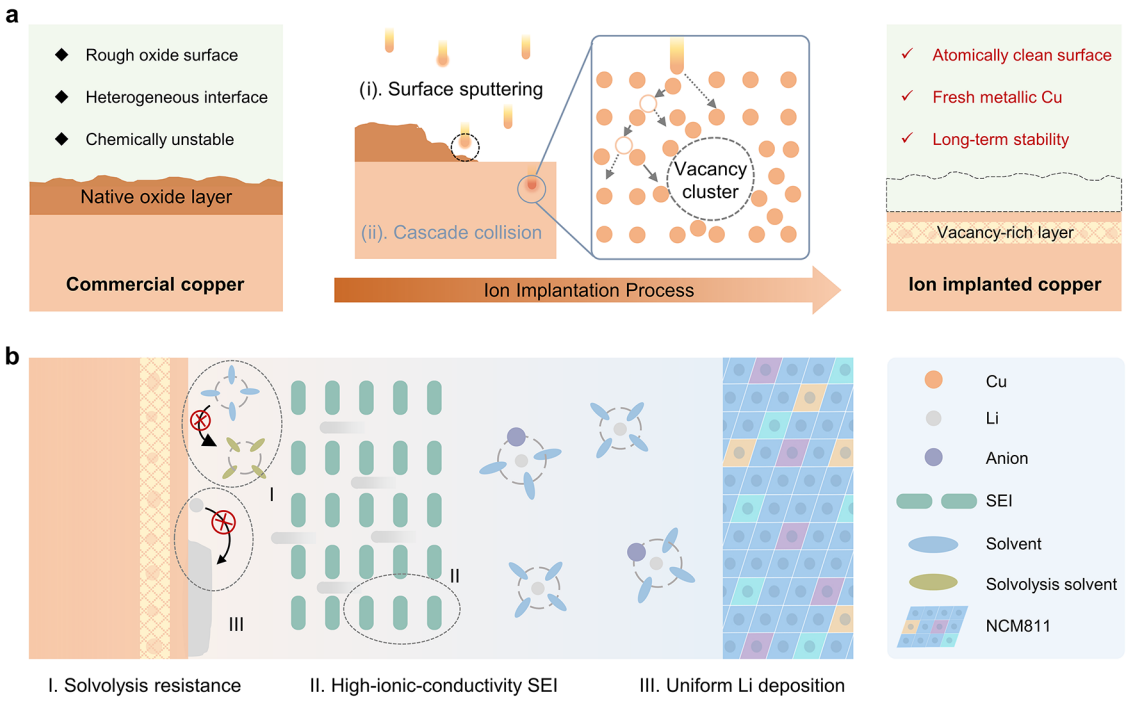


Figure 1. Schematic of the overall concept. (a) Formation mechanism of antioxidation Cu current collectors (CuCCs) with superior interfacial properties via the ion implantation process. (b) Key advantages of ion-implanted CuCCs for achieving high-performance AFLMBs.

While considerable efforts have been devoted to stabilizing this interface via electrolyte optimization,[12] three-dimensional host architectures,[13] artificial SEI layers,[14] interfacial defect engineering,[15] and surface modifications.[16] These strategies typically address interfacial manifestations rather than their fundamental origin. In particular, commercial Cu foils[17,18] develop a native oxide layer upon air exposure, which becomes the effective lithium plating interface.[19] This amorphous oxide is electronically insulating and chemically unstable, promoting heterogeneous nucleation and uncontrolled SEI evolution. Although treatments such as acid etching or thermal reduction can partially remove the oxide,[20−22] rapid reoxidation under ambient conditions remains a persistent barrier. Coating-based approaches provide some protection but often compromise conductivity or scalability.

Here, we introduce a substrate-intrinsic atomic interface engineering (AIE) strategy that employs homoelemental ion implantation to address the fundamental instabilities of anode-free lithium metal batteries. By implanting Cu ions into commercial Cu current collectors (CuCCs), this approach avoids extrinsic dopants, isolates the intrinsic energetic effects of implantation, and preserves the interfacial thickness, thereby providing an ideal platform for probing lithium−collector interactions. Ion implantation concurrently removes the native oxide and generates subsurface vacancy clusters (Figure 1a), which act as potent oxygen traps that suppress reoxidation and endow the collector with a >90 day ambient stability. Multiscale simulations and spectroscopy show that implantation drives substantial lattice reconfiguration, producing an atomically clean and chemically robust surface. Integrated into anode-free cells (cells without lithium metal at the initial state; Figure 1b), the engineered interface regulates lithium nucleation, promotes the preferential formation of a Li_2O-rich SEI, and mitigates electrolyte corrosion. This leads to an average of 98.8% Coulombic efficiency over 600 cycles under lean-electrolyte conditions. Our findings establish a scalable and robust route for engineering CuCC interfaces, resolving key degradation pathways in AFLMBs and offering a generalizable strategy for stable, high-performance anode-free architectures.

RESULTS AND DISCUSSION

Interfacial Regulation of CuCCs via Ion Implantation

The CuCC plays a critical role in AFLMBs, as it directly governs electron transport and interfacial reactions with lithium, thereby profoundly influencing the Li nucleation behavior, interfacial stability, and overall electrochemical performance. Here, we employ Cu-ion implantation to treat commercial Cu foils for precise interfacial regulation, achieving controlled Li nucleation and enhanced interfacial stability. To the best of our knowledge, this work represents the first demonstration of homoelemental ion-implanted CuCCs for high-performance battery applications, as schematically illustrated in Figure 1a. Although ion implantation has been widely used to enhance corrosion and wear resistance in metals and to modify the surfaces of ceramics and semiconductors,[23,24] its potential for constructing battery interfaces remains largely unexplored.

During the ion implantation process, accelerators impart high kinetic energy to ions, which bombard the material surface and induce complex physical and chemical transformations. In our system, accelerated Cu ions strike the Cu foil surface, sputter away the native oxide layer, penetrate into the near-surface region, and generate vacancy defects beneath the surface (Figure 1a). Distinct from conventional additive deposition techniques,[25] such as physical vapor deposition (PVD) or atomic layer deposition (ALD), this ion-implantation approach constructs a vacancy-enriched interfacial structure without altering the foil thickness or

https://doi.org/10.1021/acsnano.6c02968
ACS Nano 2026, 20, 18688−18699

Downloaded from pubs.acs.org/ancac3/article-pdf/20/26/18688/6518791/acsnano.6c02968.pdf by PEKING UNIV user on 06 November 2026

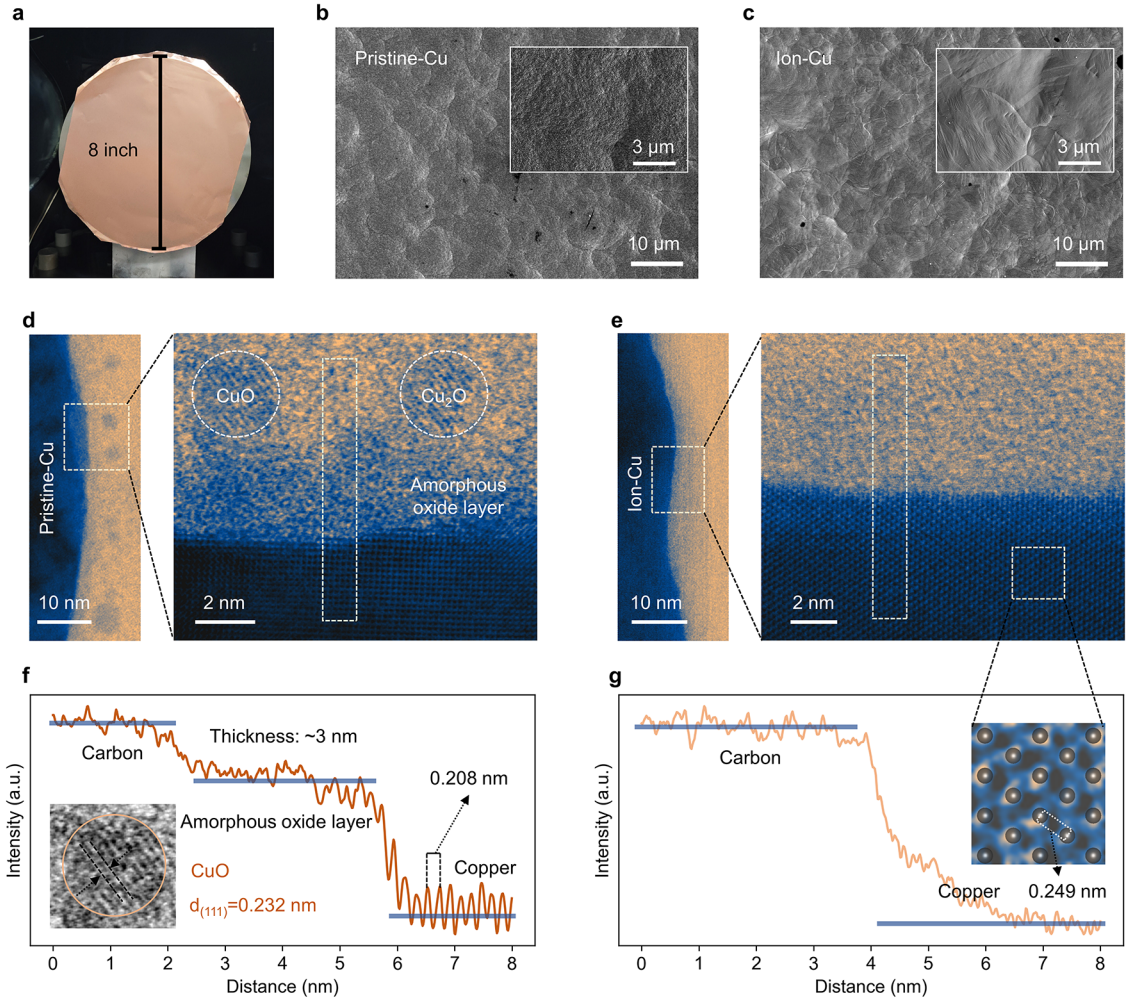


Figure 2. Surface cleaning via ion implantation on Cu foils. (a) Photograph of the ion implantation process on Cu foils. (b, c) Top-view SEM images of Pristine-Cu (b) and Ion-Cu (c), with insets showing magnified regions that highlight surface morphology differences. (d, e) Cross-sectional HRTEM images of Pristine-Cu (d) and Ion-Cu (e), showing the presence and absence of a native oxide layer, respectively. (f, g) Magnified HRTEM images and intensity profiles of regions highlighted in (d, e).

compromising the intrinsic electrical conductivity and mechanical integrity of Cu. Instead, it maintains a chemically "fresh" Cu surface by trapping oxygen via vacancy sites, thereby suppressing surface reoxidation.

Ion implantation primarily generates two effects: the mass effect and the energy effect.[24,26] To eliminate doping-related complications associated with the mass effect, we employed Cu-ion implantation, ensuring that the implanted ions were chemically identical to the substrate. Benefiting from the milliampere-range beam current provided by a metal vapor vacuum arc (MEVVA) source,[27] the entire implantation process was completed within 25 min. Notably, the implantation area reached 8 in. in diameter, enabling the simultaneous treatment of Cu foils sufficient for fabricating approximately 300 coin-sized cell current collectors (Figure 2a), highlighting the strong potential of this strategy for scalable and industrially relevant applications.

To comprehensively elucidate the effects of ion implantation on Cu current collectors, we systematically examined the morphology, crystallography, and surface chemistry of Cu foils subjected to different treatments, namely, pristine Cu (Pristine-Cu), acid-treated Cu, and ion-implanted Cu (Ion-Cu). Scanning electron microscopy (SEM) images reveal that Ion-Cu exhibits a smoother and more uniform surface morphology compared to Pristine-Cu (Figure 2b,c). Electron backscattered diffraction (EBSD) orientation maps show similar grain size, shape, and crystallographic orientation between the two foils (Supporting Figure 1). X-ray diffraction (XRD) patterns confirm that the overall crystallographic texture remains unchanged. However, the increased full width at half-maximum (fwhm) of the diffraction peaks indicates a higher density of lattice defects in Ion-Cu (Supporting Figure 2). Cross-sectional high-resolution transmission electron microscopy (HRTEM) further highlights these structural differences: Pristine-Cu displays a three-layer structure comprising an amorphous carbon layer, an oxide layer (~2−3 nm, CuO/Cu_2O), and a bulk Cu layer, whereas Ion-Cu presents a two-layer structure consisting only of carbon and Cu (Figure 2d−g and Supporting Figure 3). The carbon layer was introduced as a protective coating during focused ion beam (FIB) milling. The absence of surface oxide in Ion-Cu was further corroborated by time-of-flight secondary ion mass spectrometry (TOF-SIMS) measurements (Supporting Figure 4).

X-ray photoelectron spectroscopy (XPS) was used to quantitatively compare the oxidation levels among Pristine-

Downloaded from pubs.acs.org/ancac3/article-pdf/20/26/18688/6518791/acsnano.6c02968.pdf by PEKING UNIV user on 06 November 2026

https://doi.org/10.1021/acsnano.6c02968
ACS Nano 2026, 20, 18688−18699

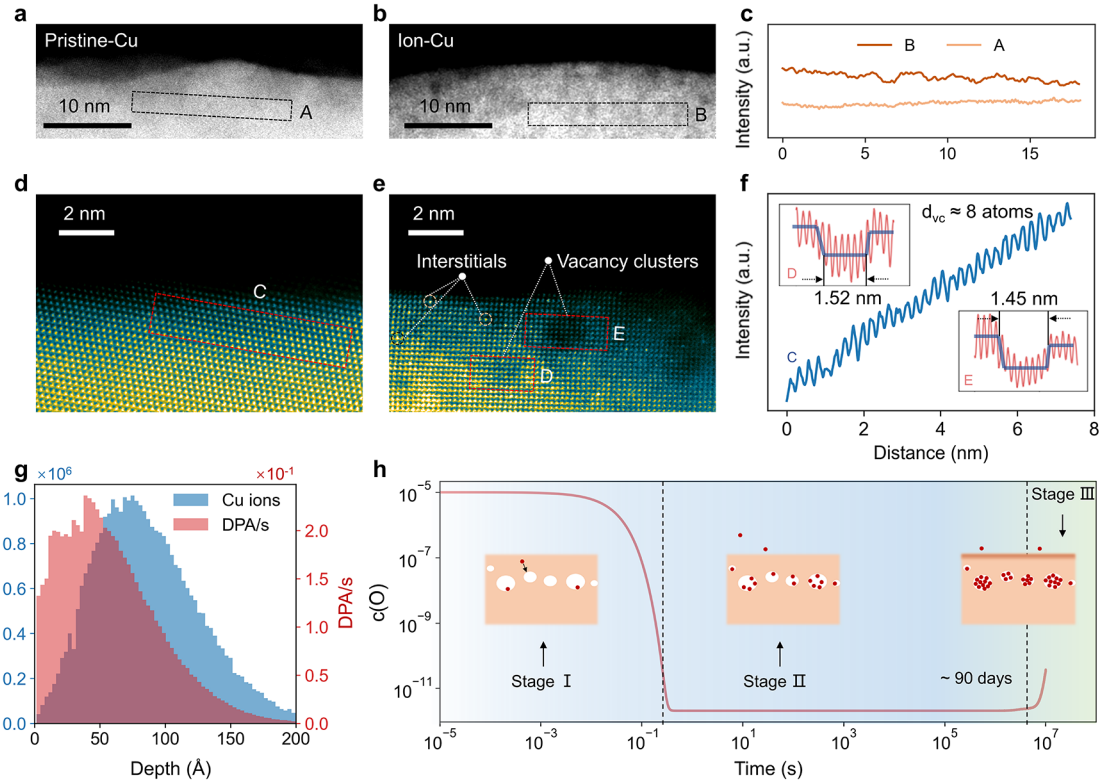


Figure 3. Subsurface vacancy formation via ion implantation on Cu foils and its effect on oxidation resistance. (a, b) Dark-field HRTEM images of Pristine-Cu (a) and Ion-Cu (b). (c) Intensity profiles of regions highlighted in (a, b). (d, e) Atomic-scale HRTEM images of Pristine-Cu (d) and Ion-Cu (e), showing nanoscale vacancy clusters and interstitial defects in Ion-Cu. (f) Intensity profiles of selected regions: Box C in Pristine-Cu and Boxes D and E in Ion-Cu. (g) TRIM simulation results showing depth distribution of implanted Cu ions (blue curve) and displacements per atom (dpa s^{-1}, red curve). (h) Simulated evolution of lattice oxygen concentration, showing three distinct stages.

Cu, acid-treated Cu, and Ion-Cu, based on the percentage area of the divalent Cu peaks at 935.44 and 955.24 eV[28,29] (Supporting Figure 5). Ion-Cu exhibited a substantially lower oxidation level than the pristine sample and a slightly lower level than its acid-treated counterpart. Four-point probe measurements further demonstrate that Ion-Cu has a significantly lower and more uniform surface resistance across the test area (Supporting Figure 6), with an average resistance of 1.59 ± 0.04 Ω (coefficient of variation [C.V.]: 2.70%) compared to 2.28 ± 0.35 Ω (C.V.: 15.31%) for Pristine-Cu.

Collectively, these results demonstrate that Ion-Cu achieves a smoother surface morphology, higher defect density, enhanced electronic conductivity, and long-term chemical stability relative to Pristine-Cu. The primary driver for the enhanced performance is the elimination of chemical and electronic heterogeneity. The "roughness" observed on Pristine-Cu is largely symptomatic of the nonuniform, insulating amorphous oxide layer. By removing this layer, Ion-Cu achieves a chemically homogeneous metallic surface with uniform electronic conductivity, which is the dominant factor in suppressing localized high-current-density hotspots and facilitating uniform Li nucleation. While acid etching can similarly remove the native oxide, it cannot prevent rapid reoxidation and generates chemical waste. By contrast, the MEVVA-based ion implantation process operates at room temperature without chemical reagents, treats large areas in a single batch, and modifies the existing substrate without altering its dimensions.

The stability of the interface in designed CuCCs is another critical parameter for practical battery applications. We examined the long-term interfacial stability of acid-treated Cu and Ion-Cu, as shown in Supporting Information Figure 5. Ion-Cu exhibited minimal degradation even after 90 days, whereas the acid-treated sample rapidly reoxidized upon air exposure, reverting to its initial state.

To elucidate the mechanism underlying the enhanced oxidation resistance of Ion-Cu, we conducted dark-field TEM measurements and multiscale simulations. Figure 3a,b present low-magnification dark-field TEM images of Pristine-Cu and Ion-Cu, respectively, while Figure 3c displays intensity profiles corresponding to the highlighted regions (boxes A and B). A notable increase in contrast roughness is observed in Ion-Cu, indicating that ion implantation introduces substantial lattice damage. HRTEM images (Figure 3d,e) further reveal atomic-scale details: Pristine-Cu exhibits a highly ordered lattice structure, whereas Ion-Cu contains numerous bright spots and regions of reduced contrast. The bright spots may correspond to interstitial Cu atoms, while the circular regions likely represent nanoscale vacancy clusters. Figure 3f presents intensity profiles of box C (Pristine-Cu) and boxes D and E (Ion-Cu). The periodic oscillations reflect an underlying Cu lattice. Box C shows a gradual intensity increase due to FIB-induced thickness variations, whereas boxes D and E reveal distinct features corresponding to vacancy clusters, with measured diameters of 1.52 and 1.45 nm, equivalent to clusters containing approximately eight Cu atoms. These vacancy clusters are identified as localized regions where

Downloaded from pubs.acs.org/ancac3/article-pdf/20/26/18688/6518791/1/acsnano.6c02968.pdf by PEKING UNIV user on 06 November 2026

https://doi.org/10.1021/acsnano.6c02968
ACS Nano 2026, 20, 18688−18699

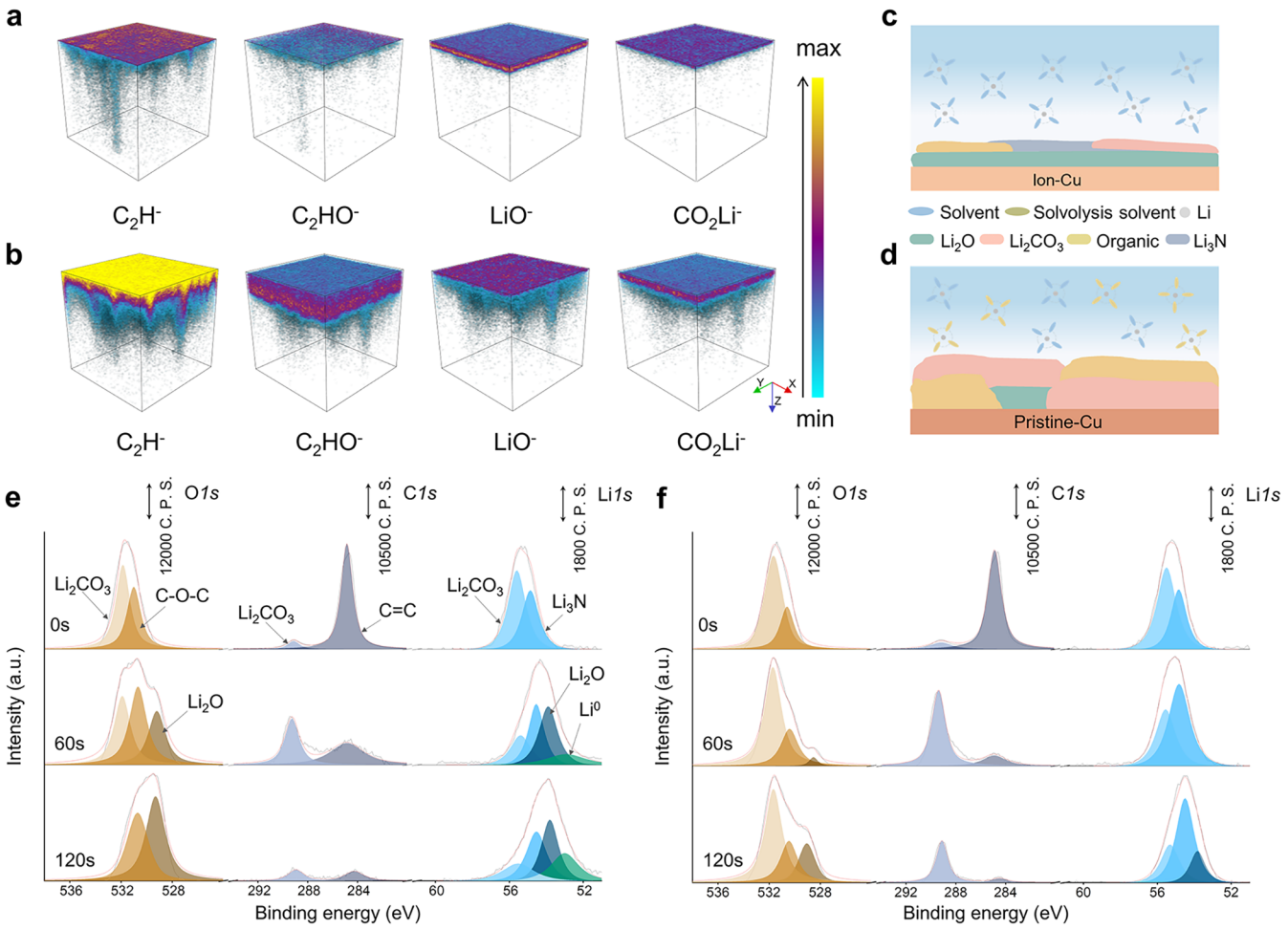


Figure 4. SEI composition on different CuCCs. (a, b) 3D-rendered TOF-SIMS images of the SEI on Ion-Cu (a) and Pristine-Cu (b) at applied potentials approaching the Li^0-metal potential (0 V vs Li/Li^+) under Cs^+ sputtering. (c, d) Depth-resolved XPS spectra (O 1s, C 1s, and Li 1s) of the SEI on the deposited Li on Ion-Cu (c) and Pristine-Cu (d). The SEI evolution on Ion-Cu and Pristine-Cu surfaces under potentials approaching Li^0-metal (0 V vs Li/Li^+). (e, f) Schematic diagrams of SEI structures on Ion-Cu (e) and Pristine-Cu (f).

multiple adjacent atomic columns exhibit uniformly diminished intensity, and the observed dimensions are consistent with the size distribution predicted by the CD simulations.

To quantitatively characterize the ion-implantation-induced defects, Monte Carlo (MC) simulations were performed to assess damage accumulation, and density functional theory (DFT) calculations were used to evaluate the binding energies between vacancies and oxygen atoms. These results were incorporated into a cluster dynamics (CD) model to simulate the evolution of vacancy clusters and the corresponding lattice oxygen concentrations (Supporting Information Figure 7).

Figure 3g illustrates the MC simulation results for ion implantation under the experimental conditions, obtained using the Transport of Ions in Matter (TRIM) module. The simulated target consisted of a 3 nm oxide layer atop a 27 nm Cu layer according to the commercial Cu foil case. The blue curve (left axis) shows the depth distribution of implanted Cu ions (normalized count), reflecting the ion concentration profile along the depth direction, with a mean stopping depth of approximately 7 nm. The red curve (right axis) displays the displacement-per-atom rate (dpa s^{-1}), quantifying the frequency of atomic displacements caused by collisions between incident ions and lattice atoms. The dpa s^{-1} profile peaks at ~5 nm beneath the surface. After subtracting the oxide layer thickness, the peak displacement depth shifts to ~2 nm, consistent with the defect-rich region observed in Figure 3e. These results confirm that the vacancy cluster formation is beneath the Cu surface but confined to a shallow depth (<0.2% of the total foil thickness), thereby preserving the macroscopic dimensions of the battery. The Bragg peak profile inherent to ion implantation concentrates lattice displacement at subsurface depths, while the topmost surface retains a relatively well-ordered crystalline structure (Figure 2e), suggesting that the vacancy-mediated oxygen-trapping function is spatially confined beneath the electrode−electrolyte interface.

To assess this effect, DFT calculations were performed on 20 representative structures containing varying numbers of vacancies and oxygen atoms (Supporting Figure 8). We systematically quantified the binding energetics for both oxygen capture (Supporting Figure 9a) and vacancy accumulation (Supporting Figure 9b). These thermodynamic parameters were fitted to analytical functions (eqs 1 and 2, see Methods). Finally, with the TRIM and DFT results serving as critical inputs, CD simulations were conducted under experimental conditions. These simulations reveal that vacancy defects tend to aggregate into nanoscale clusters (Supporting Figure 9c). The resulting cluster size distribution peaks at approximately 50 atoms, corresponding to a diameter of ~1.0 nm. This is slightly smaller than the experimentally observed clusters (~1.4 nm in diameter), possibly due to limited

https://doi.org/10.1021/acsnano.6c02968
ACS Nano 2026, 20, 18688−18699

Downloaded from pubs.acs.org/ancac3/article-pdf/20/26/18688/6518791 1/acsnano.6c02968.pdf by PEKING UNIV user on 06 November 2026

resolution of HRTEM imaging or thermally enhanced vacancy migration during ion implantation. Further CD simulations examined the evolution of lattice oxygen concentrations. Assuming an initial lattice oxygen concentration of 10^{-5} and oxygen production rates set (P_O) of 1×10^{-9} s^{-1}, Figure 3h depicts a three-stage process. In Stage 1, residual lattice oxygen is rapidly captured by vacancy clusters, reducing its concentration below 10^{-12} within one second. Stage 2 represents the antioxidation phase, during which newly generated lattice oxygen (from surface adsorption) is efficiently trapped by vacancies,[30,31] maintaining a near-zero oxygen concentration. In Stage 3, the saturation of vacancy clusters leads to the gradual reappearance of lattice oxygen. It should be noted that varying P_O affects the duration of each stage but does not alter the underlying physical processes. The selected P_O value aligns with experimental observations showing that Ion-Cu begins to exhibit slight oxidation after 90 days. This time scale is corroborated by the acid-treated Cu control, which shares an initially oxide-free surface but lacks subsurface vacancies and reoxidizes within days (Supporting Figure 5b), confirming that the sustained antioxidation behavior of Ion-Cu originates from the vacancy-mediated oxygen trapping rather than oxide removal alone.

SEI Formation on Ion-Implanted CuCCs

The formation and evolution of the solid electrolyte interphase (SEI) on CuCCs are critical determinants of the interfacial stability and cycling reversibility in AFLMBs. In conventional CuCCs, nonuniform Li nucleation and continuous surface reoxidation often lead to inhomogeneous SEI growth, repeated SEI rupture, and an excessive amount of electrolyte consumption. By contrast, the vacancy-enriched surface created via ion implantation fundamentally alters the interfacial chemistry and nucleation behavior, thereby regulating the SEI formation from the initial plating stage.

TOF-SIMS and XPS measurements were performed to compare the SEI evolution on Ion-Cu and Pristine-Cu surfaces (Figure 4). As shown in Figure 4a,b, the SEI formed on Ion-Cu is significantly thinner than that on Pristine-Cu. Additionally, the Ion-Cu SEI exhibits markedly reduced signals from organic species (e.g., C_2H^- and C_2HO^-), indicative of suppressed solvent decomposition. XPS analysis reveals the atomic concentrations at various depths for SEI formed on different CuCCs (Supporting Figure 10). At every etching stage, the SEI on Ion-Cu exhibits lower carbon (C) and oxygen (O) contents and a higher proportion of inorganic Li species compared to that on Pristine-Cu, showing the formation of a thinner, denser SEI layer. Detailed analysis of the O 1s spectra shows contributions from Li_2CO_3, C−O−C, and Li_2O species. With increasing etching depth, a greater abundance of Li_2O is detected on Ion-Cu, whereas Li_2CO_3 remains dominant on Pristine-Cu (Figure 4c,d). Given that Li_2CO_3 is unstable in direct contact with Li metal and prone to react, forming amorphous LiC_x,[32] its accumulation leads to SEI thickening, continuous electrolyte depletion, and degradation of electrochemical performance. Moreover, Li_2CO_3 imposes the highest diffusion barrier among SEI inorganic components, hindering Li^+ transport.[33] In contrast, on Ion-Cu, the Li_2O layer envelops residual Li_2CO_3 (Figure 4e,f), effectively isolating it from direct Li-metal contact and thus mitigating side reactions. A higher presence of N-SO_x and LiN_xO_y is observed on Pristine-Cu surfaces, whereas LiN_x is more prominent on Ion-Cu surfaces, suggesting distinct decomposition pathways of electrolyte components (Supporting Figure 11).

To uncover the origin of the distinct SEI compositions between Ion-Cu and Pristine-Cu, cyclic voltammetry (CV) was conducted on the three types of Cu foils (Supporting Information Figure 5c−f). The CV results demonstrate that SEI formation proceeds through two potential-dependent stages. At 1.0 to 2.0 V vs Li/Li^+, SEI initiates via direct electron transfer (ET). In this region, Ion-Cu exhibits a higher exchange current density than acid-treated Cu, and both are substantially larger than that of Pristine-Cu, indicating that Ion-Cu and acid-treated Cu form a more robust and inorganic-rich direct-ET SEI. This trend aligns well with previous reports that high-CE electrolytes also promote an enhanced direct-ET current in this potential window.

At potentials below 0.5 V, since both acid-treated Cu and Ion-Cu already possess a stable and compact direct-ET SEI formed at 1.0 to 2.0 V, Li underpotential deposition (UPD) does not induce excessive additional SEI formation. In contrast, Pristine-Cu forms only a sparse and low-quality direct-ET SEI. Coupled with the strong affinity of surface copper oxides toward solvent molecules, Li-UPD triggers massive parasitic solvent decomposition, producing a highly organic-rich and unstable SEI.

For Pristine-Cu, persistent UPD/UPS peaks in subsequent cycles reflect continuous SEI formation and dissolution, which cause sustained Li corrosion and gradual thickening of a resistive and unstable SEI layer (Supporting Information Figure 5e). By comparison, the complete absence of UPD/UPS peaks for both acid-treated Cu and Ion-Cu confirms that their SEI layers are stable and fully established in the initial cycle, effectively protecting the Li metal anode without repeated side reactions (Supporting Information Figure 5f).

Clearly, oxide removal plays a vital role in regulating the SEI formation. Furthermore, Ion-Cu delivers a more favorable SEI composition relative to acid-treated Cu (Supporting Information Figure 5c), which agrees well with its larger exchange current in the 1.0 to 2.0 V region. The fundamental origin lies in the lower residual oxide content of Ion-Cu. In addition, the subsurface vacancy clusters, which are located beneath the surface without direct electrolyte contact, provide a durable oxygen-trapping effect that sustains an oxide-free state over a long period. This conclusion is further supported by direct immersion tests (Supporting Information Figure 11c), in which the Pristine-Cu electrolyte solution shows visible discoloration and significantly higher interfacial impedance after 12 h, whereas the Ion-Cu solution remains colorless with minimal impedance increase.

Li Plating/Stripping Behavior

Lil|Cu half-cells pairing Li foils with different CuCCs were assembled using an ether-based electrolyte (1.0 M LiTFSI in a 1:1 vol/vol mixture of DOL/DME with 5% $LiNO_3$) to evaluate the Li plating/stripping behavior. For a comprehensive comparison, oxidized Cu (Oxi-Cu) was also prepared by soaking commercial Cu foils in a 1 M NaOH solution for 24 h to achieve complete surface oxidation. Electrochemical measurements, SEM characterizations, and DFT calculations were employed to study the Li plating/stripping behavior. Benefiting from the Li_2O-rich SEI induced by ion implantation, Ion-Cu exhibits the smallest interfacial impedance (25.39 Ω) and the lowest nucleation overpotential (38.4 mV) in Lil|Cu half-cells (Supporting Figures 12−14). Ion-Cu promoted

Downloaded from pubs.acs.org/ancac3/article-pdf/20/26/18688/6518791/1/acsnano.6c02968.pdf by PEKING UNIV user on 06 November 2026

https://doi.org/10.1021/acsnano.6c02968
ACS Nano 2026, 20, 18688−18699

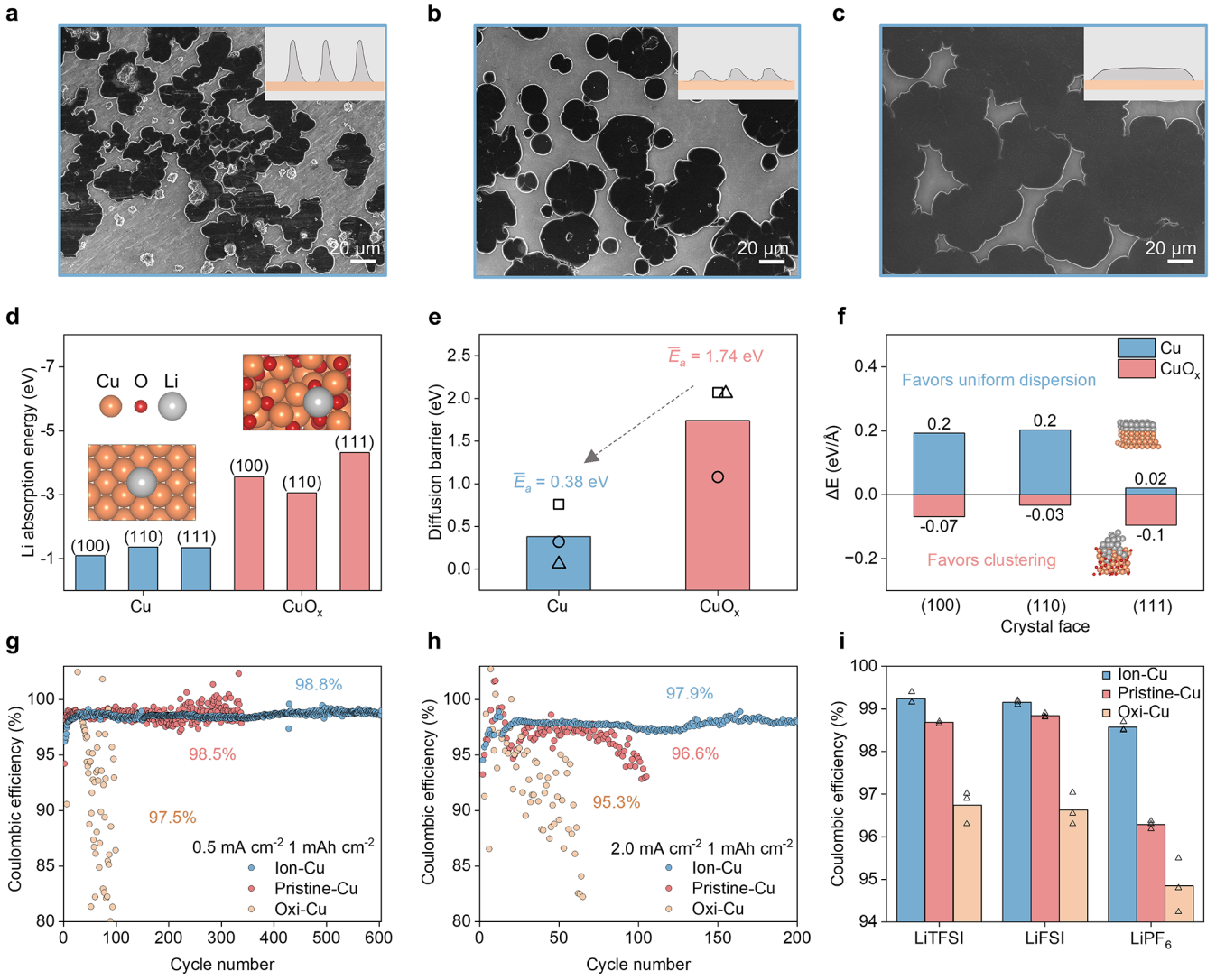


Figure 5. Li deposition morphology and electrochemical performance of Li−Cu half-cells. (a−c) SEM images of Li deposited on Oxi-Cu (a), Pristine-Cu (b), and Ion-Cu (c) with a capacity of 0.5 mAh cm^{-2} under a current density of 0.5 mA cm^{-2}. (d) Li adsorption energies on Cu and amorphous CuO_x surfaces for different facets ((100), (110), and (111)). (e) Li diffusion barriers (E_a) on Cu and CuO_x surfaces, showing significantly hindered mobility on oxidized surfaces. (f) Thermodynamic energy difference (ΔE) between clustered and dispersed Li configurations on different crystal facets. (g, h) Cycling performance of Li||Cu half-cells using different CuCCs at 0.5 mA cm^{-2} (g) and 2 mA cm^{-2} (h), both with an areal capacity of 1.0 mAh cm^{-2}. (i) Coulombic efficiency (CE) of Li||Cu half-cells measured with the Aurbach protocol using different electrolytes: 1.0 M LiTFSI in a 1:1 vol/vol mixture of DOL/DME with 5% $LiNO_3$; 1:1.8:2 mol/mol/mol LiFSI/DME/TTE; and 1.0 M $LiPF_6$ in a 1:1 vol/vol EC/DEC with 10% FEC and 1% VC additives.

nucleation sites with larger radii compared to Pristine-Cu (Supporting Figures 15−17). This optimized nucleation behavior directly translates to improved lithium deposition morphology. As the degree of surface oxidation decreased from Oxi-Cu to Ion-Cu, the deposited Li became progressively larger, denser, and less granular (Figure 5a−c). Li deposited on Ion-Cu shows a dense structure with a thickness of approximately 2.5 μm at 0.5 mAh cm^{-2} (Supporting Figure 18). Even under high current density, Ion-Cu enables densely packed, film-like Li deposition, while Oxi-Cu and Pristine-Cu exhibit pronounced dendritic Li growth (Supporting Figure 19). After stripping, Ion-Cu displays negligible dead Li, indicating its highly reversible Li plating/stripping behavior (Supporting Figure 20).

Li plating/stripping behavior was also studied by DFT calculations. Li adsorption and migration on representative metallic Cu, including (100), (110), and (111) facets, as well as on amorphous CuO_x surfaces, were investigated (Figure 5d). The amorphous CuO_x surfaces were modeled by randomly incorporating oxygen atoms into crystalline Cu slab models at a Cu:O atomic ratio of 1:1. The resulting structures were subjected to three sequential relaxation steps—geometry optimization with fixed in-plane dimensions, molecular dynamics equilibration at 300 K using the density-functional tight-binding (DFTB) method, and final geometry optimization—to obtain equilibrated amorphous configurations (see Methods in the Supporting Information for full details). The Li adsorption energies were found to be significantly lower (i.e., more thermodynamically favorable) on CuO_x surfaces compared to Cu surfaces, indicating stronger Li binding and more effective trapping at initial nucleation sites. Transition state (TS) analysis further revealed that the surface diffusion barrier for Li on CuO_x (~1.74 eV) is more than four times higher than that on metallic Cu (~0.38 eV),

https://doi.org/10.1021/acsnano.6c02968
ACS Nano 2026, 20, 18688−18699

Downloaded from pubs.acs.org/ancac3/article-pdf/20/26/18688/6518791/1/acsnano.6c02968.pdf by PEKING UNIV user on 06 November 2026

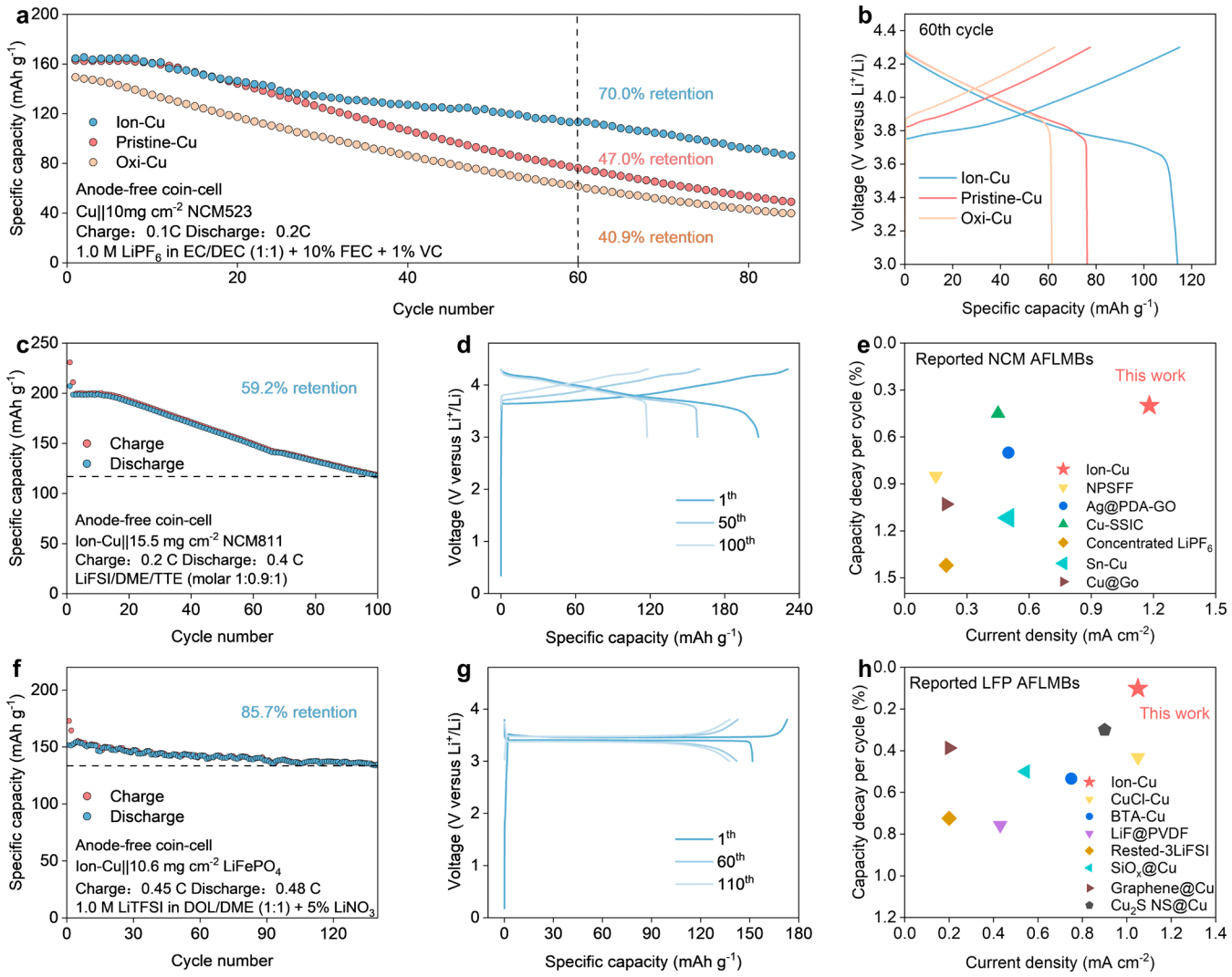


Figure 6. Electrochemical performance of full cells with different CuCCs. (a) Long-term cycling performance of anode-free Cu||NCM523 coin cells. (b) Corresponding charge/discharge profiles of the Cu||NCM523 coin cells at the 60th cycle. (c) Long-term cycling performance of anode-free Ion-Cu||NCM811 coin-cell. (d) Corresponding charge/discharge profiles of the Ion-Cu||NCM811 coin-cell at 1st, 50th, and 100th cycles. (e) Electrochemical performance comparison of AFLMBs with NCM cathode between this work and previously reported work.[34−39] (f) Long-term cycling performance of anode-free Ion-Cu||LFP coin-cell. (g) Corresponding charge/discharge profiles of the Ion-Cu||LFP coin-cell at 1st, 60th, and 110th cycles. (h) Electrochemical performance comparison of AFLMBs with LFP cathode between this work and previously reported work.[40−46]

suggesting a substantial reduction in Li migration rates on oxidized surfaces (Figure 5e). This dramatic decrease in surface mobility promotes localized Li deposition, consistent with experimental observations (Supporting Figure 21). To assess whether deposited Li atoms preferentially migrate laterally or vertically onto existing Li clusters, surface models incorporating Li steps were constructed to evaluate the corresponding energy barriers. The calculated barrier for vertical climbing (~1.32 eV) was much higher than for lateral surface diffusion (~0.38 eV), indicating a strong preference for Li to spread laterally across the Cu surface rather than to vertically accumulate (Supporting Figure 22). This lateral diffusion behavior contributes to the formation of flat and dense Li morphologies on Ion-Cu substrates. Furthermore, the energetic stability of two distinct Li deposition configurations—dispersed Li layers (M1) versus clustered Li islands (M2)—was compared on both Cu and CuO_x surfaces. We calculated the energy difference (ΔE) between clustered and dispersed states (Figure 5f). On metallic Cu, dispersed Li was energetically more favorable, while on CuO_x surfaces, clustered Li was preferred (Supporting Figure 23). These trends were further validated through ab initio molecular dynamics (AIMD) simulations (Supporting Figure 24). Interfacial formation energy calculations confirmed that dispersed Li configurations are thermodynamically favored on Cu, whereas clustering is promoted on CuO_x surfaces, except for CuO_x (111), where the upward migration of O atoms during relaxation induced anomalous behavior.

Li−Cu Half-Cell Cycling Performance

To test the half-cell performance for different CuCCs (Pristine-Cu, Oxi-Cu, and Ion-Cu), Li||Cu half-cells pairing Li foils were assembled using an ether-based electrolyte (1.0 M LiTFSI in a 1:1 vol/vol mixture of DOL/DME with 5% $LiNO_3$). Ion-Cu achieves a CE of 98.8% over 600 cycles, outperforming Pristine-Cu (98.5% over 300 cycles) and Oxi-Cu (short-circuits after only 50 cycles at 0.5 mA cm^{-2} and 1

Downloaded from pubs.acs.org/ancac3/article-pdf/20/26/18688/6518791/1/acsnano.6c02968.pdf by PEKING UNIV user on 06 November 2026

https://doi.org/10.1021/acsnano.6c02968
ACS Nano 2026, 20, 18688−18699

mAh cm^{-2}) (Figure 5g). At a higher current density of 2 mA cm^{-2}, Ion-Cu maintains a CE of 97.9% over 200 cycles (Figure 5h), while Pristine-Cu and Oxi-Cu fail after 100 and 30 cycles, respectively. When the current density is further increased to 5 mA cm^{-2}, the Ion-Cu cell reaches a high CE of 96.43% after only 2 activation cycles and remains stable above 95% over 50 cycles, whereas the CE of Pristine-Cu failed after 42 cycles with a lower average CE of 87% (Supporting Figure 25).

Moreover, Ion-Cu demonstrates consistently high average CEs of 99.23%, 99.15%, and 98.57% across different electrolyte systems with improved Li plating/stripping behaviors, underscoring the robustness of the interfacial engineering strategy (Figure 5i and Supporting Figures 26–28). The voltage profiles are presented in Supporting Figure 29, Ion-Cu exhibits the smallest polarization voltage in all electrolytes. Impressively, even in a fluorine-free ester-based electrolyte (1.0 M $LiPF_6$ in a 1:1 vol/vol mixture of EC/DEC)—which typically yields poor CE—Ion-Cu significantly improves lithium plating/stripping behavior and long-term cycling stability, demonstrating its broad applicability (Supporting Figure 30).

Full Cell Performance

To further validate the effectiveness of the vacancy-engineered interface created by ion implantation in practical battery systems, AFLMBs were fabricated by pairing Ion-Cu with various commercial cathodes, including NCM523, NCM811, and $LiFePO_4$ (LFP). These full-cell configurations provide a stringent assessment of Li reversibility and interfacial stability under the realistic operating conditions.

The Ion-Cu||NCM523 full cell delivers an impressive initial discharge capacity of 163.95 mAh g^{-1} at 0.2 C (Figure 6a), while maintaining 70.0% capacity retention over 60 cycles. This performance corresponds to a substantial 43.4% reduction in the capacity decay rate compared with cells employing Pristine-Cu (47.0%) and Oxi-Cu (40.9%) under identical conditions. The notably lower initial capacity of the Oxi-Cu cell originates from the electronically insulating nature of the intentionally thickened oxide layer, which increases interfacial charge-transfer resistance and polarization, while simultaneously consuming a larger fraction of the limited cathode-sourced lithium inventory through irreversible parasitic reactions during the first cycle (Supporting Figure 13). Voltage-capacity profiles recorded at the 60th cycle reveal significantly reduced polarization and more stable electrochemical behavior for the Ion-Cu-based cell relative to the Pristine-Cu and Oxi-Cu counterparts (Figure 6b and Supporting Figure 31). When the cycling rate is increased to 0.6 C, Ion-Cu-based AFLMBs with NCM523 cathodes still retain 42.3% of their capacity after 100 cycles (Supporting Figure 32).

When paired with a high-energy-density NCM811 cathode, the Ion-Cu AFLMB maintains a capacity retention of 59.2% after 100 cycles, accompanied by stable voltage profiles throughout cycling (Figure 6c,d). Under high mass-loading conditions (33.1 mg cm^{-2}), the performance advantage of Ion-Cu becomes even more pronounced: the Ion-Cu electrode preserves 40.2% capacity retention after 80 cycles, whereas the Pristine-Cu-based cell rapidly degrades to only 11.16% retention (Supporting Figure 33). The universality of Ion-Cu as a high-performance anode current collector was further demonstrated using commercial LFP cathodes in anode-free cells. The LFP full cells exhibit highly stable cycling behavior, maintaining 85.7% of their initial capacity over 140 cycles at a charge/discharge rate of 0.5 C/0.6 C (Figure 6f). The corresponding charge–discharge profiles show negligible potential decay over prolonged cycling (Figure 6g), indicative of a highly stable interfacial structure enabled by ion implantation. Benchmark comparisons with previously reported AFLMB systems suggest that the Ion-Cu configuration exhibits competitive robustness among reported anode-free battery architectures (Figure 6e,h).

Beyond coin-cell demonstrations, the practical viability of Ion-Cu was further validated in pouch-cell configurations. A 50 mAh prototype Ion-Cu||NCM523 AFLMB pouch cell was assembled and operated stably for 60 cycles under lean-electrolyte conditions (2.4 g Ah^{-1}) (Supporting Figures 34–35). The pouch cell achieves a high specific energy density of approximately 320 Wh kg^{-1}, highlighting the exceptional effectiveness of Ion-Cu in enhancing Li reversibility in practical AFLMBs.

CONCLUSIONS

In summary, we developed an AIE strategy to construct oxidation-resistant CuCCs for AFLMBs, starting from an anode-free cell configuration. Through Cu-ion implantation, the native amorphous oxide layer on commercial Cu foils can be effectively removed, while subsurface vacancy clusters are introduced that are capable of capturing residual oxygen atoms, as supported by multiscale experimental characterizations and simulations. The resulting oxidation-resistant Cu surface exhibits improved interfacial stability, mitigates electrolyte solvolysis, reduces and homogenizes surface resistance, and facilitates a more uniform lateral Li deposition. These interfacial modifications favor the formation of a thin, Li_2O-enriched SEI, which is associated with reduced interfacial charge-transfer resistance and enhances Li^+ transport kinetics. As a consequence, the modified CuCCs show improved electrochemical performance, including a CE of 98.8% over 600 cycles in Li–Cu half-cells and 85.7% capacity retention after 140 cycles in full-cell configurations with LFP cathodes. This work suggests that ion implantation is a versatile approach for the interfacial engineering of CuCCs. Owing to its compatibility with large-area processing, short treatment time, and direct applicability to commercial Cu foils without altering the bulk structure, the proposed strategy may offer a practical route toward improving the performance and reliability of the AFLMBs.

METHODS

Preparation of Ion-Cu

Ion-Cu was prepared by implanting Cu ions into commercial Cu foils (MSK-WTMC–CU2G) at room temperature using a FAD-MEVVA ion implanter, whose beam spot exceeds 8 in. in diameter and allowed simultaneous treatment of foils sufficient for more than 300 current collectors. The ion fluence was varied from 10^{13} to 10^{16} ions cm^{-2} and the ion energy from 5 to 20 keV; unless otherwise stated, all electrochemical measurements used the optimized condition of 9 keV and 1×10^{16} ions cm^{-2}. Full details are provided in the Supporting Information.

Preparation of Acid-Treated Cu

Commercial Cu foils were immersed in 1.0 M CH_3COOH for 10 min at room temperature, rinsed with deionized water and ethanol, dried under argon, and transferred to an argon-filled glovebox before use.

Downloaded from pubs.acs.org/ancac3/article-pdf/20/26/18688/6518791/acsnano.6c02968.pdf by PEKING UNIV user on 06 November 2026

https://doi.org/10.1021/acsnano.6c02968
ACS Nano 2026, 20, 18688–18699

Electrochemical Measurements

Cells were assembled as 2032-type coin cells with a Celgard 2325 separator in an argon-filled glovebox (O_2 and H_2O below 0.01 ppm). Li||Cu half-cells used Li foil as the counter electrode, and Coulombic efficiencies were determined by the Aurbach method. Anode-free full cells (Ion-Cu||NCM523, ≈10 mg cm^{-2}) and pouch cells were activated at 0.05 C between 3.0 and 4.3 V (1 C = 165 mA g^{-1}) and subsequently cycled at 0.1−0.2 C. Unless otherwise stated, the electrolyte was 1 M LiTFSI in DOL/DME (1:1 by volume) with 5 wt % $LiNO_3$. Additional electrolytes and protocols are described in the Supporting Information.

Characterizations

Surface morphology was examined by scanning electron microscopy (SEM, Hitachi S-4800). X-ray photoelectron spectroscopy (XPS) was performed on a Kratos AXIS Ultra spectrometer with monochromatic Al Kα radiation, with binding energies calibrated to the C 1s peak at 284.6 eV. Crystallography was assessed by X-ray diffraction (XRD, Rigaku SmartLab, Cu Kα) and electron backscattered diffraction (EBSD, eFlash HR). Samples for SEI analysis were rinsed with anhydrous DME and transferred under vacuum to avoid air exposure.

Computational Methods

Multiscale modeling combined Monte Carlo (TRIM) simulations of implantation damage, density functional theory (DFT) calculations of vacancy−oxygen energetics, and cluster-dynamics simulations of vacancy-cluster and lattice-oxygen evolution. Lithium adsorption and diffusion on crystalline and amorphous Cu and CuO_x surfaces were evaluated by DFT, complemented by ab initio and density-functional tight-binding molecular dynamics. Full parameters, codes, and associated references are provided in the Supporting Information.

■ ASSOCIATED CONTENT

Data Availability Statement

The data that support the findings of this study are available in the main text and Supporting Information. All relevant data are available from the corresponding authors upon request.

Supporting Information

The Supporting Information is available free of charge at https://pubs.acs.org/doi/10.1021/acsnano.6c02968.

Experimental and computational methods; supplementary SEM, EBSD, GIXRD, and HRTEM characterization; TOF-SIMS and XPS depth-profiling of the SEI; multiscale simulation (TRIM, DFT, cluster dynamics) details; supplementary electrochemical performance (Figures S1−S35) and (Tables S1−S2) (PDF)

■ AUTHOR INFORMATION

Corresponding Authors

Yusheng Ye − *Beijing Key Laboratory of Environmental Science and Engineering, School of Materials Science and Engineering, Beijing Institute of Technology, Beijing 100081, China;* orcid.org/0000-0001-9832-2478; Email: ysye@bit.edu.cn

Ziqiang Zhao − *School of Materials Science and Engineering, Peking University, Beijing 100871, China; State Key Laboratory of Nuclear Physics and Technology, School of Physics, Peking University, Beijing 100871, China;* orcid.org/0000-0002-5557-9094; Email: zqzhao@pku.edu.cn

Xin Gao − *School of Materials Science and Engineering, Peking University, Beijing 100871, China;* orcid.org/0000-0001-5360-0796; Email: gaoxin-cnc@pku.edu.cn

Jin Zhang − *School of Materials Science and Engineering, Peking University, Beijing 100871, China; Beijing National Laboratory for Molecular Sciences, College of Chemistry and Molecular Engineering, Peking University, Beijing 100871, China;* orcid.org/0000-0003-3731-8859; Email: jinzhang@pku.edu.cn

Authors

Yue Li − *School of Materials Science and Engineering, Peking University, Beijing 100871, China; State Key Laboratory of Nuclear Physics and Technology, School of Physics, Peking University, Beijing 100871, China;* orcid.org/0000-0002-3972-0692

Xuanguang Ren − *School of Materials Science and Engineering, Peking University, Beijing 100871, China; Beijing National Laboratory for Molecular Sciences, College of Chemistry and Molecular Engineering, Peking University, Beijing 100871, China*

Xueting Feng − *Beijing National Laboratory for Molecular Sciences, College of Chemistry and Molecular Engineering, Peking University, Beijing 100871, China*

Lingcheng Kong − *School of Materials Science and Engineering, Peking University, Beijing 100871, China*

Fengping Luo − *State Key Laboratory of Nuclear Physics and Technology, School of Physics, Peking University, Beijing 100871, China*

Yang Xu − *State Key Laboratory of Nuclear Physics and Technology, School of Physics, Peking University, Beijing 100871, China*

Liu Qian − *School of Materials Science and Engineering, Peking University, Beijing 100871, China*

Complete contact information is available at: https://pubs.acs.org/10.1021/acsnano.6c02968

Author Contributions

⊥Y.L., X.R., X.F., and L.K. contributed equally to this work.

Notes

A previous version of this manuscript was deposited as a preprint: Li, Y.; Ren, X.; Feng, X.; Kong, L.; Luo, F.; Xu, Y.; Qian, L.; Ye, Y.; Zhao, Z.; Gao, X.; and Zhang, J. Atomic Interface Engineering of Battery Current Collectors via Ion Implantation. 2025, arXiv:2508.00236. arXiv. 10.48550/arXiv.2508.00236 (accessed June 5, 2026).

The authors declare no competing financial interest.

■ ACKNOWLEDGMENTS

This work was financially supported by the Ministry of Science and Technology of China (2022YFA1203302, 2022YFA1203304, and 2025YFE0211900), the National Natural Science Foundation of China (52302034, 52021006, 52102032, 52272033, 52402041), the Scientific Research Innovation Capability Support Project for Young Faculty (SRICSPYF-ZY2025066), the Strategic Priority Research Program of CAS (XDB36030100), the Beijing National Laboratory for Molecular Sciences (BNLMS-CXTD-202001), and the Shenzhen Science and Technology Innovation Commission (KQTD20221101115627004).

■ REFERENCES

(1) Magnussen, O. M.; Groß, A. Toward an Atomic-Scale Understanding of Electrochemical Interface Structure and Dynamics. *J. Am. Chem. Soc.* **2019**, *141*, 4777−4790.

(2) Irvine, J. T. S.; Neagu, D.; Verbraeken, M. C.; Chatzichristodoulou, C.; Graves, C.; Mogensen, M. B. Evolution of

Downloaded from pubs.acs.org/ancac3/article-pdf/20/26/18688/6518791/acsnano.6c02968.pdf by PEKING UNIV user on 06 November 2026

the Electrochemical Interface in High-Temperature Fuel Cells and Electrolysers. *Nat. Energy* **2016**, *1*, No. 15014.
(3) Li, C.; Shao, Q.-G.; Luo, K.; Gao, Y.-Q.; Zhao, W.-W.; Cao, N.; Du, S.-Y.; Jin, X.; Zou, P.-C.; Zang, X.-B. A Lean-Zinc and Zincophilic Anode for Highly Reversible Zinc Metal Batteries. *Adv. Funct. Mater.* **2023**, *33*, No. 2305204.
(4) Nanda, S.; Gupta, A.; Manthiram, A. Anode-Free Full Cells: A Pathway to High-Energy Density Lithium-Metal Batteries. *Adv. Energy Mater.* **2021**, *11*, No. 2000804.
(5) Weber, R.; Genovese, M.; Louli, A. J.; Hames, S.; Martin, C.; Hill, I. G.; Dahn, J. R. Long Cycle Life and Dendrite-Free Lithium Morphology in Anode-Free Lithium Pouch Cells Enabled by a Dual-Salt Liquid Electrolyte. *Nat. Energy* **2019**, *4*, 683−689.
(6) Heubner, C.; Maletti, S.; Auer, H.; Hüttl, J.; Voigt, K.; Lohrberg, O.; Nikolowski, K.; Partsch, M.; Michaelis, A. From Lithium-Metal toward Anode-Free Solid-State Batteries: Current Developments, Issues, and Challenges. *Adv. Funct. Mater.* **2021**, *31*, No. 2106608.
(7) Huang, W.; Zhao, C.; Wu, P.; Yuan, H.; Feng, W.; Liu, Z.; Lu, Y.; Sun, S.; Fu, Z.; Hu, J.; Yang, S.; Huang, J.; Zhang, Q. Anode-Free Solid-State Lithium Batteries: A Review. *Adv. Energy Mater.* **2022**, *12*, No. 2201044.
(8) Fang, C.; Lu, B.; Pawar, G.; Zhang, M.; Cheng, D.; Chen, S.; Ceja, M.; Doux, J.-M.; Musrock, H.; Cai, M.; Liaw, B.; Meng, Y. S. Pressure-Tailored Lithium Deposition and Dissolution in Lithium Metal Batteries. *Nat. Energy* **2021**, *6*, 987−994.
(9) Lin, D.; Liu, Y.; Cui, Y. Reviving the Lithium Metal Anode for High-Energy Batteries. *Nat. Nanotechnol.* **2017**, *12*, 194−206.
(10) Wang, H.; Yu, Z.; Kong, X.; Kim, S. C.; Boyle, D. T.; Qin, J.; Bao, Z.; Cui, Y. Liquid Electrolyte: The Nexus of Practical Lithium Metal Batteries. *Joule* **2022**, *6*, 588−616.
(11) Yuan, X.; Liu, B.; Mecklenburg, M.; Li, Y. Ultrafast Deposition of Faceted Lithium Polyhedra by Outpacing SEI Formation. *Nature* **2023**, *620*, 86−91.
(12) Zhang, E.; Chen, Y.; Holoubek, J.; Yu, Z.; Zhang, W.; Lyu, H.; Choi, I. R.; Kim, S. C.; Serrao, C.; Cui, Y.; Bao, Z. Monofluorinated Acetal Electrolyte for High-Performance Lithium Metal Batteries. *Proc. Natl. Acad. Sci. U.S.A.* **2025**, *122*, No. e2418623122.
(13) Kwon, H.; Lee, J.-H.; Roh, Y.; Baek, J.; Shin, D. J.; Yoon, J. K.; Ha, H. J.; Kim, J. Y.; Kim, H.-T. An Electron-Deficient Carbon Current Collector for Anode-Free Li-Metal Batteries. *Nat. Commun.* **2021**, *12*, No. 5537.
(14) Zhai, P.; Wang, T.; Jiang, H.; Wan, J.; Wei, Y.; Wang, L.; Liu, W.; Chen, Q.; Yang, W.; Cui, Y.; Gong, Y. 3D Artificial Solid-Electrolyte Interphase for Lithium Metal Anodes Enabled by Insulator−Metal−Insulator Layered Heterostructures. *Adv. Mater.* **2021**, *33*, No. 2006247.
(15) Zhao, H.; Du, S.; Liu, Q.; Liu, X.; Lu, D.; Liu, T.; Yin, Y.; Li, Y.; Zou, P.; Wu, Z. Defective Interface Customizes Anion-Aggregated Helmholtz Plane for Anode-Less Lithium Metal Batteries. *ACS Nano* **2025**, *19*, 34942−34953.
(16) Lu, G.; Liu, W.; Yang, Z.; Wang, Y.; Zheng, W.; Deng, R.; Wang, R.; Lu, L.; Xu, C. Superlithiophilic, Ultrastable, and Ionic-Conductive Interface Enabled Long Lifespan All-Solid-State Lithium-Metal Batteries under High Mass Loading. *Adv. Funct. Mater.* **2023**, *33*, No. 2304407.
(17) Kim, S. J.; Kim, Y. I.; Lamichhane, B.; Kim, Y.-H.; Lee, Y.; Cho, C. R.; Cheon, M.; Kim, J. C.; Jeong, H. Y.; Ha, T.; Kim, J.; Lee, Y. H.; Kim, S.-G.; Kim, Y.-M.; Jeong, S.-Y. Flat-Surface-Assisted and Self-Regulated Oxidation Resistance of Cu(111). *Nature* **2022**, *603*, 434−438.
(18) Yang, J. C.; Kolasa, B.; Gibson, J. M.; Yeadon, M. Self-Limiting Oxidation of Copper. *Appl. Phys. Lett.* **1998**, *73*, 2841−2843.
(19) Yoon, J. S.; Liao, D. W.; Greene, S. M.; Cho, T. H.; Dasgupta, N. P.; Siegel, D. J. Thermodynamics, Adhesion, and Wetting at Li/Cu(-Oxide) Interfaces: Relevance for Anode-Free Lithium−Metal Batteries. *ACS Appl. Mater. Interfaces* **2024**, *16*, 18790−18799.
(20) Lee, S. Y.; Mettlach, N.; Nguyen, N.; Sun, Y. M.; White, J. M. Copper Oxide Reduction through Vacuum Annealing. *Appl. Surf. Sci.* **2003**, *206*, 102−109.
(21) Qu, G.; Vegunta, S. S. S.; Mai, K.; Weinman, C. J.; Ghosh, T.; Wu, W.; Flake, J. C. Copper Oxide Removal Activity in Nonaqueous Carboxylic Acid Solutions. *J. Electrochem. Soc.* **2013**, *160*, No. E49.
(22) Chavez, K. L.; Hess, D. W. A Novel Method of Etching Copper Oxide Using Acetic Acid. *J. Electrochem. Soc.* **2001**, *148*, G640−G643.
(23) Li, W.; Zhan, X.; Song, X.; Si, S.; Chen, R.; Liu, J.; Wang, Z.; He, J.; Xiao, X. A Review of Recent Applications of Ion Beam Techniques on Nanomaterial Surface Modification: Design of Nanostructures and Energy Harvesting. *Small* **2019**, *15*, No. 1901820.
(24) Nastasi, M.; Mayer, J. W. *Ion Implantation and Synthesis of Materials*; Springer: Berlin, Heidelberg, 2006.
(25) Xu, R.; Cheng, X.-B.; Yan, C.; Zhang, X.-Q.; Xiao, Y.; Zhao, C.-Z.; Huang, J.-Q.; Zhang, Q. Artificial Interphases for Highly Stable Lithium Metal Anode. *Matter* **2019**, *1*, 317−344.
(26) Wright, G. M.; Barnard, H. A.; Kesler, L. A.; Peterson, E. E.; Stahle, P. W.; Sullivan, R. M.; Whyte, D. G.; Woller, K. B. An Experiment on the Dynamics of Ion Implantation and Sputtering of Surfaces. *Rev. Sci. Instrum.* **2014**, *85*, No. 023503.
(27) Zhang, T.; Wang, X.; Liang, H.; Zhang, H.; Zhou, G.; Sun, G.; Zhao, W.; Xue, J. Behaviour of MEVVA Metal Ion Implantation for Surface Modification of Materials. *Surf. Coat. Technol.* **1996**, *83*, 280−283.
(28) Iijima, J.; Lim, J.-W.; Hong, S.-H.; Suzuki, S.; Mimura, K.; Isshiki, M. Native Oxidation of Ultra High Purity Cu Bulk and Thin Films. *Appl. Surf. Sci.* **2006**, *253*, 2825−2829.
(29) Zuo, Z.-J.; Li, J.; Han, P.-D.; Huang, W. XPS and DFT Studies on the Autoxidation Process of Cu Sheet at Room Temperature. *J. Phys. Chem. C* **2014**, *118*, 20332−20345.
(30) McColl, K.; Coles, S. W.; Zarabadi-Poor, P.; Morgan, B. J.; Islam, M. S. Phase Segregation and Nanoconfined Fluid O2 in a Lithium-Rich Oxide Cathode. *Nat. Mater.* **2024**, *23*, 826−833.
(31) Kilic, M. E.; Lee, J.-H.; Lee, K.-R. Oxygen Ion Transport in Doped Ceria: Effect of Vacancy Trapping. *J. Mater. Chem. A* **2021**, *9*, 13883−13889.
(32) Han, B.; Zhang, Z.; Zou, Y.; Xu, K.; Xu, G.; Wang, H.; Meng, H.; Deng, Y.; Li, J.; Gu, M. Poor Stability of Li2CO3 in the Solid Electrolyte Interphase of a Lithium-Metal Anode Revealed by Cryo-Electron Microscopy. *Adv. Mater.* **2021**, *33*, No. 2100404.
(33) Zhao, Q.; Stalin, S.; Archer, L. A. Stabilizing Metal Battery Anodes through the Design of Solid Electrolyte Interphases. *Joule* **2021**, *5*, 1119−1142.
(34) Zhan, J.; Deng, L.; Liu, Y.; Hao, M.; Wang, Z.; Dong, L.; Yang, Y.; Song, K.; Qi, D.; Wang, J.; Wang, S.; Liu, H.; Zhou, W.; Chen, H. Self-Selective (220) Directional Grown Copper Current Collector Design for Cycling-Stable Anode-Less Lithium Metal Batteries. *Adv. Mater.* **2025**, *37*, No. 2413420.
(35) Wondimkun, Z. T.; Tegegne, W. A.; Jiang, S.-K.; Huang, C.-J.; Sahalie, N. A.; Weret, M. A.; Hsu, J.-Y.; Hsieh, P.-L.; Huang, Y.-S.; Wu, S.-H.; Su, W.-N.; Hwang, B. J. Highly-Lithiophilic Ag@PDA-GO Film to Suppress Dendrite Formation on Cu Substrate in Anode-Free Lithium Metal Batteries. *Energy Storage Mater.* **2021**, *35*, 334−344.
(36) Oyakhire, S. T.; Zhang, W.; Shin, A.; Xu, R.; Boyle, D. T.; Yu, Z.; Ye, Y.; Yang, Y.; Raiford, J. A.; Huang, W.; Schneider, J. R.; Cui, Y.; Bent, S. F. Electrical Resistance of the Current Collector Controls Lithium Morphology. *Nat. Commun.* **2022**, *13*, No. 3986.
(37) Hagos, T. T.; Thirumalraj, B.; Huang, C.-J.; Abrha, L. H.; Hagos, T. M.; Berhe, G. B.; Bezabh, H. K.; Cherng, J.; Chiu, S.-F.; Su, W.-N.; Hwang, B.-J. Locally Concentrated LiPF6 in a Carbonate-Based Electrolyte with Fluoroethylene Carbonate As a Diluent for Anode-Free Lithium Metal Batteries. *ACS Appl. Mater. Interfaces* **2019**, *11*, 9955−9963.
(38) Zhang, S. S.; Fan, X.; Wang, C. A Tin-Plated Copper Substrate for Efficient Cycling of Lithium Metal in an Anode-Free Rechargeable Lithium Battery. *Electrochim. Acta* **2017**, *258*, 1201−1207.
(39) Wondimkun, Z. T.; Beyene, T. T.; Weret, M. A.; Sahalie, N. A.; Huang, C.-J.; Thirumalraj, B.; Jote, B. A.; Wang, D.; Su, W.-N.; Wang, C.-H.; Brunklaus, G.; Winter, M.; Hwang, B.-J. Binder-Free Ultra-Thin Graphene Oxide As an Artificial Solid Electrolyte Interphase for

Downloaded from pubs.acs.org/ancac3/article-pdf/20/26/18688/6518791/1/acsnano.6c02968.pdf by PEKING UNIV user on 06 November 2026

https://doi.org/10.1021/acsnano.6c02968
ACS Nano 2026, 20, 18688−18699

Anode-Free Rechargeable Lithium Metal Batteries. *J. Power Sources* **2020**, *450*, No. 227589.
(40) Li, Z.; Huang, X.; Kong, L.; Qin, N.; Wang, Z.; Yin, L.; Li, Y.; Gan, Q.; Liao, K.; Gu, S.; Zhang, T.; Huang, H.; Wang, L.; Luo, G.; Cheng, X.; Lu, Z. Gradient Nano-Recipes to Guide Lithium Deposition in a Tunable Reservoir for Anode-Free Batteries. *Energy Storage Mater.* **2022**, *45*, 40−47.
(41) Kang, T.; Zhao, J.; Guo, F.; Zheng, L.; Mao, Y.; Wang, C.; Zhao, Y.; Zhu, J.; Qiu, Y.; Shen, Y.; Chen, L. Dendrite-Free Lithium Anodes Enabled by a Commonly Used Copper Antirusting Agent. *ACS Appl. Mater. Interfaces* **2020**, *12*, 8168−8175.
(42) Tamwattana, O.; Park, H.; Kim, J.; Hwang, I.; Yoon, G.; Hwang, T.; Kang, Y.-S.; Park, J.; Meethong, N.; Kang, K. High-Dielectric Polymer Coating for Uniform Lithium Deposition in Anode-Free Lithium Batteries. *ACS Energy Lett.* **2021**, *6*, 4416−4425.
(43) Chen, W.; Salvatierra, R. V.; Ren, M.; Chen, J.; Stanford, M. G.; Tour, J. M. Laser-Induced Silicon Oxide for Anode-Free Lithium Metal Batteries. *Adv. Mater.* **2020**, *32*, No. 2002850.
(44) Assegie, A. A.; Chung, C.-C.; Tsai, M.-C.; Su, W.-N.; Chen, C.-W.; Hwang, B.-J. Multilayer-Graphene-Stabilized Lithium Deposition for Anode-Free Lithium-Metal Batteries. *Nanoscale* **2019**, *11*, 2710−2720.
(45) Yang, Z.; Liu, W.; Chen, Q.; Wang, X.; Zhang, W.; Zhang, Q.; Zuo, J.; Yao, Y.; Gu, X.; Si, K.; Liu, K.; Wang, J.; Gong, Y. Ultrasmooth and Dense Lithium Deposition toward High-Performance Lithium-Metal Batteries. *Adv. Mater.* **2023**, *35*, No. 2210130.
(46) Zhang, Q.-K.; Zhang, X.-Q.; Wan, J.; Yao, N.; Song, T.-L.; Xie, J.; Hou, L.-P.; Zhou, M.-Y.; Chen, X.; Li, B.-Q.; Wen, R.; Peng, H.-J.; Zhang, Q.; Huang, J.-Q. Homogeneous and Mechanically Stable Solid−Electrolyte Interphase Enabled by Trioxane-Modulated Electrolytes for Lithium Metal Batteries. *Nat. Energy* **2023**, *8*, 725−735.

Downloaded from pubs.acs.org/ancac3/article-pdf/20/26/18688/6518791 1/acsnano.6c02968.pdf by PEKING UNIV user on 06 November 2026

https://doi.org/10.1021/acsnano.6c02968
ACS Nano 2026, 20, 18688−18699